ACCSCIENCE PUBLISHING

International Journal of Bioprinting

ACCEPTED PAPER · MAIN TEXT

Ta/PEEK cages with enhanced hydrophilicity and cell adhesion improve intervertebral fusion in a rabbit XLIF model

Paper version: Accepted Paper

Accepted Papers are manuscripts accepted for publication, encompassing all changes made following the peer review process, along with a standard cover page indicating the paper version and an "Accepted Paper" watermark, but excluding any other editing, typesetting or other changes made by AccScience Publishing and/or authors post-acceptance.

Article ID: IJB026140127

Citation: Li S, Wu H, Gao H, *et al*. Ta/PEEK cages with enhanced hydrophilicity and cell adhesion improve intervertebral fusion in a rabbit XLIF model. *Int J Bioprint*. 2026. doi: 10.36922/IJB026140127

Copyright: © 2026 Author(s). This is an Open Access article distributed under the terms of the Creative Commons Attribution License, permitting distribution, and reproduction in any medium, provided the original work is properly cited.

Publisher's Note: AccScience Publishing remains neutral with regard to jurisdictional claims in published maps and institutional affiliations.

AccScience Publishing
RESEARCH ARTICLE
Volume X Issue X (2026)
doi: 10.36922/IJB026140127

Ta/PEEK cages with enhanced hydrophilicity and cell adhesion improve intervertebral fusion in a rabbit XLIF model

Shaorong Li, Han Wu, Hongwei Gao, Jianshi Song, Xiuqi Shan, Jiaqi Li, Lei Ma, and Wei Zhang*

Department of Spinal Surgery, The Third Hospital of Hebei Medical University, Shijiazhuang, 050001, Hebei, China

***Corresponding author:**
Wei Zhang (37300332@hebmu.edu.cn)

Citation: Li S, Wu H, Gao H, *et al*. Ta/PEEK cages with enhanced hydrophilicity and cell adhesion improve intervertebral fusion in a rabbit XLIF model. *Int J Bioprint.* 2026. doi: 10.36922/IJB026140127

Received: April 1, 2026
Revised: June 7, 2026
Accepted: June 15, 2026
Published online: June 15, 2026

Copyright: © 2026 Author(s). This is an Open-Access article distributed under the terms of the Creative Commons Attribution License, permitting distribution, and reproduction in any medium, provided the original work is properly cited.

Publisher's Note: AccScience Publishing remains neutral with regard to jurisdictional claims in published maps and institutional affiliations.

ACCEPTED PAPER

Abstract

This study developed bioactive cages by fabricating hydroxyapatite-coated titanium (HA/Ti) and tantalum-coated PEEK (Ta/PEEK) cages and evaluated their physicochemical properties, cellular responses, and intervertebral fusion performance in a rabbit XLIF model. Both coatings improved surface wettability and maintained the intrinsic mechanical properties of the substrates. Ta/PEEK showed superior coating adhesion and enhanced BMSC adhesion-related marker expression, whereas HA/Ti more strongly promoted osteogenic differentiation and matrix mineralization in vitro. In vivo, both coated cages significantly improved intervertebral fusion compared with uncoated Ti and PEEK cages. HA/Ti induced greater new bone formation, while Ta/PEEK enhanced cell adhesion and angiogenesis, as indicated by increased CDH1, ITGα2, CD31 and HIF-1α expression. These findings suggest that Ta/PEEK cages provide a mechanically compatible and biologically active strategy for improving intervertebral fusion and represent a promising platform for next-generation printed spinal implants.

Keywords: Cage; Hydroxyapatite; Intervertebral fusion; PEEK; Tantalum; XLIF

ACCEPTED PAPER

1. Introduction

Lumbar degenerative disorders are increasingly prevalent with population aging and remain a major cause of disability and healthcare expenditure worldwide[1-3]. Lumbar intervertebral fusion remains one of the most widely adopted surgical interventions for the treatment of degenerative spinal pathologies, aiming to achieve adequate neural decompression and durable biomechanical stabilization through successful osseous fusion[4]. Among various surgical approaches, extreme lateral intervertebral fusion (XLIF) has emerged as an effective minimally invasive technique for treating degenerative disc disease, spondylolisthesis, adjacent segment degeneration, and related spinal disorders. By enabling the placement of larger intervertebral cages while preserving posterior paraspinal musculature, XLIF facilitates restoration of disc height and lumbar lordosis, reduces the risk of cage subsidence, and may contribute to improved long-term clinical outcomes[5]. However, because XLIF relies primarily on implant-mediated fusion rather than extensive autologous bone grafting, the biological performance of the implanted cage becomes a critical determinant of surgical success.

As the primary load-bearing and fusion-promoting component, the intervertebral cage plays a pivotal role in restoring spinal alignment, maintaining immediate postoperative stability, reducing instrumentation failure, and facilitating bone bridging between adjacent vertebral bodies[6,7]. Consequently, the biological and mechanical characteristics of the bone–implant interface profoundly influence fusion outcomes. Despite widespread clinical use, conventional titanium (Ti) and polyether ether ketone (PEEK) cages exhibit intrinsic limitations[8,9]. Titanium implants possess excellent biocompatibility and favorable osteoconductive potential; however, their relatively high elastic modulus and radiodensity may contribute to stress shielding, implant subsidence, and difficulties in radiographic assessment. In contrast, PEEK exhibits mechanical properties closer to those of native bone and superior radiolucency, yet its bioinert surface often results in insufficient osseointegration and delayed fusion[10].

To overcome these limitations, extensive efforts have been devoted to surface engineering strategies that enhance implant bioactivity without compromising the desirable bulk properties of the substrate materials. Current approaches include morphological modification, deposition of bioactive coatings, and incorporation of therapeutic biomolecules[11-13]. Among these, bioactive surface coatings have attracted considerable attention because they can substantially improve

ACCEPTED PAPER

osteogenic performance while preserving the mechanical integrity of the underlying implant[14]. Hydroxyapatite (HA), owing to its close compositional similarity to the mineral phase of bone, has been extensively utilized to promote protein adsorption, osteoblast activity, and osteoconduction[15]. Nevertheless, the chemically inert and smooth surface of PEEK limits stable HA immobilization and increases the risk of coating delamination under physiological loading conditions[16,17]. In contrast, metallic substrates generally provide stronger coating adhesion and superior long-term stability.

Among the emerging coating materials, tantalum (Ta) has attracted increasing interest because of its excellent biocompatibility, corrosion resistance, and exceptional osteogenic activity. Ta-based surface modification has therefore been proposed as a promising strategy for overcoming the biological limitations of PEEK while preserving its favorable mechanical characteristics[18]. However, systematic preclinical comparisons of clinically relevant coating strategies remain scarce, largely owing to the high cost and technical complexity of large-animal fusion models[19]. In this study, HA/Ti and Ta/PEEK intervertebral cages were engineered and evaluated through integrated physicochemical characterization, in vitro BMSC assays, and in vivo validation in a rabbit XLIF model. By directly comparing Ta/PEEK with clinically established HA/Ti cages, we sought to clarify how Ta surface modification alters the biological performance of PEEK and whether this strategy can improve intervertebral fusion. This work provides preclinical evidence for the rational design of bioactive spinal implants and establishes a practical small-animal platform for screening next-generation cage materials.

2. Materials and methods

2.1. Materials

Ti6Al4V and PEEK was supplied and processed by AK Medical holdings Limited (Beijing, China). Hydroxyapatite (HA) was purchased from Aladdin Biochemical Technology Co., Ltd (Shanghai, China). Cell culture plates and dishes for cell experiments were purchased from Corning Company in New York, USA. Low-sugar DMEM medium, fetal bovine serum(FBS), 0.25% EDTA, penicillin and streptomycin were purchased from Gibco (New York, USA). Primary antibodies against Runx-2, OCN, CD31, HIF-1α, CDH1 and ITGα2 were purchased from Proteintech Group co., ltd(Wuhan, China).

ACCEPTED PAPER

2.2. Preparation of coated cage

The cages used in this study were supplied by Beijing Aikang Technology Co., Ltd. and fabricated via Fused Deposition Modeling (FDM) and Selective Laser Melting (SLM) using a Factory Ultra system. Guided by prior research and the anatomical structure of rabbit spines, cage dimensions were tailored to meet experimental requirements. Specifically, implants featured a a rectangular prism geometry (1.5 mm × 2 mm × 10 mm). The printing parameters were set as follows: laser power, 90 W; scanning speed, 700 mm/min; and layer thickness, 25 μm. The entire fabrication process was conducted under a high-purity argon atmosphere, with the oxygen content in the chamber rigorously maintained below 80 ppm to minimize metal oxidation.

Following fabrication, all cages underwent systematic post-processing. To thoroughly remove residual powder, support structures, and contaminants, the cages were sequentially ultrasonically cleaned in acetone, anhydrous ethanol, and deionized water (three cycles per solvent, 60 minutes per cycle). To enhance their bioactivity, the cages were subsequently coated with HA and Ta. The HA coating was applied by immersing the sintered cages in an HA suspension under vacuum for 2 minutes to ensure complete infiltration of the porous structure. Finally, the samples were dried at room temperature for 3 hours to allow solvent evaporation and formation of a uniform HA layer. Ta coatings were deposited using a filtered cathodic arc source equipped with a 99.99% pure Ta target. Prior to plasma immersion ion implantation, the chamber pressure was reduced to 5×10^{-3} Pa. Argon gas was introduced into the cathode arc source at a flow rate of 5 sccm to maintain stable Ta ionization. PEEK samples were mounted on a rotating stage connected to a high-voltage pulse generator. A pulsed negative high voltage was applied to drive Ta ions into the sample surfaces, with continuous rotation ensuring uniform implantation. Following the surface treatments, samples were sterilized by autoclaving at 121°C for 20 minutes, dried in an oven at 60°C, and finally subjected to ultraviolet (UV) irradiation for surface cleaning.

2.3. Characterization of cages

2.3.1. Morphology and composition

The surface morphology of the cages was characterized using scanning electron microscopy (SEM, SU-8100, Hitachi, Japan). Prior to observation, all samples were ultrasonically cleaned, thoroughly dried, and sputter-coated with a thin layer of gold to improve electrical conductivity.

ACCEPTED PAPER

SEM imaging was performed at an accelerating voltage of 5 kV to examine the surface microstructure and porous architecture of the cages.

Elemental composition and distribution were analyzed using energy-dispersive X-ray spectroscopy (EDS, FEI TECNAI G2 F30, USA). Elemental mapping and semi-quantitative compositional analyses were conducted to evaluate the spatial distribution and relative abundance of coating-associated elements.

The surface chemical composition and elemental valence states of the coatings were analyzed using X-ray photoelectron spectroscopy (XPS, ESCALAB Xi+, Thermo Fisher Scientific, USA) with monochromatic Al Kα radiation (hν = 1486.6 eV). Both survey spectra and high-resolution spectra were acquired under constant analyzer pass-energy conditions. All spectra were charge-corrected using the C 1s peak at 284.8 eV as the reference. High-resolution spectra of Ta 4f, Ca 2p, and P 2p were deconvoluted and fitted using Avantage software (Thermo Fisher Scientific, USA) to determine the corresponding chemical states of the surface elements.

2.3.2. Porosity of cages

The porosity of the cages was determined using the liquid displacement method. The initial volume (V0) and weight (W0) of the samples were precisely measured. The samples were then immersed in absolute ethanol, and their weights were monitored at intervals of 1, 5, 10, 20, 40, and 60 minutes to ensure complete saturation. This process continued until a constant mass was achieved, denoted as W1. The porosity of the cages was calculated according to the following equation:

Porosity (%) = $(W_1 - W_0) / (\rho \times V_0) \times 100\%$ (where ρ represents the density of ethanol.)

2.3.3. Contact Angle

Surface wettability was assessed using a static water contact-angle analyzer (Model G10, Kruss, Germany). Measurements were conducted by depositing a 2.5 μL droplet of deionized water onto the surface of each sample.

2.3.4. Mechanical Properties

The mechanical properties of the cages were evaluated using a universal testing machine (Model 5567, Instron, USA). Compression tests were conducted in accordance with the ISO

ACCEPTED PAPER

13314:2011 standard. Specimens were compressed at 1 mm min^{-1} until failure, and compressive strength and elastic modulus were derived from the stress–strain curves. The compressive strength and elastic modulus were calculated from the resulting stress-strain curves.

2.3.5. Coating performance

The thickness of the surface coatings was determined using a focused ion beam/scanning electron microscopy (FIB–SEM) system (Helios G4, FEI, USA). Cross-sections were prepared using a Ga^+ ion beam operated at 30 kV and 1 nA, followed by final polishing at 0.1 nA. Coating thickness was directly measured from high-magnification cross-sectional SEM images. Surface roughness was quantified using a three-dimensional optical profilometer (Contour GT-K, Bruker, USA) operating in vertical scanning interferometry mode. Surface topography was acquired over an area of 500 × 500 μm^2 with a vertical resolution of 0.1 nm and a lateral resolution of 0.5 μm. After Gaussian filtering (cutoff wavelength λc = 0.08 mm), the arithmetic average roughness (Ra) and maximum height (Rz) were calculated. The interfacial adhesion strength of the coatings was evaluated using a scratch tester (Revetest Xpress, Anton Paar, Switzerland) equipped with a Rockwell C diamond stylus (tip radius: 200 μm). Progressive loading from 0 to 50 N was applied at a loading rate of 10 N min^{-1} over a scratch length of 5 mm. The critical load (Lc_2), corresponding to the onset of cohesive or adhesive coating failure, was determined from acoustic emission and tangential force signals.

2.4. In vitro experiments

2.4.1. Cell viability, proliferation, and morphology

BMSCs were isolated from 1-week-old Sprague-Dawley (SD) rats and cultured in low-glucose DMEM supplemented with 10% FBS and 1% penicillin-streptomycin. The cells were maintained in an incubator (Thermo Fisher Scientific, Shanghai, China) at 37°C with 5% CO_2. BMSCs at the third passage were used for all subsequent cellular experiments. Subsequent in vitro investigations were performed by co-culturing BMSCs with Ti, HA/Ti, PEEK, and Ta/PEEK cages to systematically evaluate their cytocompatibility and osteogenic potential (Cells were seeded around and in contact with each cage to evaluate cage-mediated effects on cytocompatibility and cellular activity). Cellular viability, proliferation, morphology, osteogenic differentiation,

ACCEPTED PAPER

extracellular matrix mineralization, and osteogenesis-related gene expression were comprehensively assessed.

Cell proliferation was assessed on days 1, 3, and 7 using a Cell Counting Kit-8 (CCK-8; Biosharp, Shanghai, China). Briefly, BMSCs were seeded in 48-well plates at a density of 3×10^3 cells per well and cultured with the following groups: Ti, PEEK, Ta/PEEK and HA/Ti cages. After 1, 3, and 7 days of incubation, 100 μL of CCK-8 solution was added to each well and incubated in the dark for approximately 3 hours. The supernatant was then collected, and the absorbance was measured at 450 nm using a microplate reader (Thermo Fisher Scientific, Shanghai, China).

The biocompatibility of the cages was assessed using a Calcein-AM/PI double-staining kit (Biosharp, Shanghai, China). BMSCs were seeded in 24-well plates at a density of 6×10^3 cells/well and cultured for 1 and 3 days. At each time point, the cells were incubated with the staining solution in the dark for 30 minutes. Following incubation, the solution was removed, and the samples were washed with PBS and observed under a fluorescence microscope (Olympus, Japan).

Additionally, BMSC morphology was evaluated using F-actin/DAPI staining (Bioss Biotechnology Co., Ltd., Beijing, China). BMSCs were seeded in 24-well plates at a density of 6×10^3 cells/well and cultured for 3 days. After discarding the culture medium and rinsing with PBS, the cells were fixed with 4% paraformaldehyde for 15 minutes. The cells were then incubated with a 5 μg/mL phalloidin solution for 30 minutes, washed with PBS, and subsequently stained with DAPI (1:1000 dilution) in the dark for 5 minutes. Finally, the samples were washed and imaged using a fluorescence microscope.

2.4.2. Alkaline phosphatase activity

BMSCs were seeded as described previously. Following cell adhesion, the culture medium was replaced with osteogenic induction medium supplemented with 50 mM ascorbic acid, 10 mM β-glycerophosphate, and 100 nM dexamethasone (Beyotime Biotechnology, Shanghai, China). After 7 days of induction, alkaline phosphatase (ALP) staining was performed to evaluate early osteogenic differentiation. The cells were washed three times with PBS and fixed with 4% paraformaldehyde for 15 minutes. Subsequently, an ALP chromogenic substrate was added according to the manufacturer's instructions, followed by incubation for 30 minutes. Staining results were observed under an optical microscope.

ACCEPTED PAPER

Furthermore, ALP activity was quantitatively measured using an Alkaline Phosphatase Activity Assay Kit (Beyotime Biotechnology, Shanghai, China). Cells from each group were washed three times with PBS and lysed with ice-cold lysis buffer. Standards, substrates, and samples were added to a 96-well plate as directed by the manufacturer, and the reaction was carried out at 37°C for 30 minutes. After adding the stop solution, the absorbance was measured at a wavelength of 405 nm. ALP activity was calculated and subjected to statistical analysis.

2.4.3. Alizarin red staining

Following 14 days of co-culture, the in vitro mineralization capacity of BMSCs was evaluated using an Alizarin Red S (ARS) staining kit (Biosharp, Shanghai, China). The samples were fixed with 4% paraformaldehyde for 30 minutes and subsequently incubated with ARS staining solution for approximately 1 hour to visualize calcium nodule formation. After washing three times with PBS to remove excess dye, the samples were imaged under an optical microscope. For quantitative analysis, 10% cetylpyridinium chloride solution was added to each well to dissolve the stained mineral deposits. The absorbance was then measured at a wavelength of 540 nm using a microplate reader.

2.4.4. RT-qPCR

Total RNA was extracted from BMSCs cultured on different cages after 7 and 14 days using TRIzol reagent (Invitrogen, USA). RNA concentration and purity were determined using a NanoDrop 2000 spectrophotometer (Thermo Fisher Scientific, USA). Subsequently, 1 μg of total RNA was reverse-transcribed into complementary DNA (cDNA) using PrimeScript RT Master Mix (Takara, Japan). Quantitative real-time PCR was performed using TB Green Premix Ex Taq II on a CFX96 Touch Real-Time PCR System (Bio-Rad, USA). Relative gene expression levels of ITGα2, CDH1, Runx-2, and OCN were normalized to GAPDH and calculated using the 2^−ΔΔCt method. All reactions were performed in triplicate. The primer sequences used for RT-qPCR are listed in **Table. 1**.

2.4.5. Immunofluorescence staining

BMSCs were seeded into 96-well plates at a density of 1×10^4 cells per well and cultured under osteogenic induction conditions for 7 days. Following induction, the culture medium was removed, and the cells were fixed with 4% paraformaldehyde for 15 min at room temperature. The

ACCEPTED PAPER

cells were subsequently permeabilized with 0.1% Triton X-100 in PBS for 10 min and blocked with 5% bovine serum albumin (BSA) in PBS at 37 °C for 30 min to minimize nonspecific binding.

The samples were then incubated overnight at 4 °C with primary antibodies against CDH1, ITGα2, Runx-2, and OCN, diluted in blocking buffer according to the manufacturers' instructions. After three washes with PBS, the cells were incubated with the corresponding fluorophore-conjugated secondary antibodies for 1 h at room temperature in the dark. Cell nuclei were counterstained with DAPI (1 μg mL^{-1}) for 5 min. Fluorescence images were acquired using a fluorescence microscope or a high-content imaging system. To eliminate potential cross-reactivity between antibodies, independent wells were prepared and processed separately for each primary antibody.

2.5. In vivo experiments

2.5.1. Preparation of intervertebral fusion model

All animal experiments were approved by the Animal Care and Use Committee of Hebei Medical University and conducted in accordance with international animal welfare guidelines (Ethical number: Z2025-046-1). Twenty-four female New Zealand white rabbits, 2 months of age, were randomly assigned to four groups (n = 6 per group). The rabbits were randomly divided into four groups (n=6 per group) and anesthetized via intravenous injection of 3% sodium pentobarbital (50 mg/kg) into the marginal ear vein. Following preoperative skin preparation and disinfection, a longitudinal incision was made over the L4–L5 intervertebral space. The paravertebral muscles were dissected along the lateral border of the sacrospinalis and quadratus lumborum to expose the L4 and L5 vertebrae. The L4/L5 intervertebral space was identified, the annulus fibrosus was incised, and the nucleus pulposus was removed. Subsequently, Ti, HA/Ti, PEEK and Ta/PEEK cages were implanted into the disc space. A two-hole plate was placed horizontally over the L4 and L5 vertebrae and secured with screws. The surgical site was thoroughly irrigated, and the wound was closed in layers with sterile dressings applied. Postoperatively, penicillin (40,000 U/kg) was administered intramuscularly for 3 consecutive days to prevent infection. All rabbits were euthanized 12 weeks post-surgery, and spinal specimens were harvested and fixed in 4% paraformaldehyde for subsequent analysis. All surgical procedures were performed by the same experienced spine surgeon (>10 years of clinical experience) assisted by a dedicated surgical team.

ACCEPTED PAPER

Identical surgical techniques and perioperative management protocols were applied to all animals to ensure consistency and reproducibility of the experimental model.

2.5.2. Radiographic fusion assessment

Intervertebral fusion was independently evaluated by three experienced spine surgeons who were blinded to the experimental groups. Fusion status was assessed using computed tomography (CT) imaging in combination with manual evaluation of intervertebral motion in the harvested specimens. Fusion was graded according to a previously validated scoring system as follows: Grade 0, absence of bridging bone with obvious intervertebral motion (nonunion); Grade 1, partial bridging bone with questionable motion (unstable union); Grade 2, definite bridging bone with minor residual gaps or incomplete consolidation (stable union with minor defects); and Grade 3, solid bridging bone characterized by continuous trabecular architecture across the intervertebral space and no detectable motion during flexion–extension testing (complete fusion). The final fusion score for each specimen was calculated as the mean of the three independent evaluations. An average score of ≥2 was defined as successful fusion.

2.5.3. Micro-CT

At 12 weeks post-surgery, osseointegration within the intervertebral region was evaluated using micro-CT (SkyScan 1076, Kontich, Belgium). Scanning was performed with a voxel size of 18.26 μm, a voltage of 48 kV, and a current of 200 μA. The acquired images were reconstructed into three-dimensional models. The region of interest (ROI) was anatomically delineated between the superior and inferior vertebral endplates of the adjacent two vertebrae, with the left and right margins confined to the bilateral boundaries of the implanted cage. Quantitative analysis was subsequently conducted using the associated analysis software to calculate the bone volume fraction (BV/TV), bone mineral density (BMD), and trabecular number (Tb.N).

2.5.4. Histological analysis

In addition to micro-CT evaluation, osseointegration in the intervertebral region was further assessed using hematoxylin and eosin (H&E) staining. At 12 weeks post-surgery, spinal specimens were harvested, fixed in 4% paraformaldehyde, and embedded in resin. Hard tissue sections with a thickness of 20 μm were prepared from the embedded blocks and subjected to H&E staining.

ACCEPTED PAPER

The stained sections were visualized under a digital microscope (DSX 500, Olympus, Tokyo, Japan), and the area of newly formed bone was quantified using ImageJ software.

2.5.5. Immunohistochemical staining

After 12 weeks of implantation, harvested vertebral specimens were fixed in 4% paraformaldehyde, decalcified, dehydrated, and embedded in paraffin. Serial sections (4 μm) were prepared for immunohistochemical analysis. Briefly, the sections were deparaffinized, rehydrated, and subjected to antigen retrieval. Endogenous peroxidase activity was blocked, followed by incubation with primary antibodies against osteogenic markers (Runx-2 and OCN) and angiogenic markers (CD31 and HIF-1α) at 4°C overnight. After washing, the sections were incubated with appropriate HRP-conjugated secondary antibodies, and the immunoreactivity was visualized using a DAB substrate kit. Finally, the sections were counterstained with hematoxylin, dehydrated, and mounted for microscopic observation. Immunohistochemical staining was semi-quantitatively analyzed using ImageJ software by measuring the positive staining area in a blinded manner.

2.5.6. In vivo biosafety evaluation

At 4 weeks postoperatively, the systemic biosafety of the implanted cages was comprehensively evaluated in all experimental animals. Following overnight fasting, blood samples were collected from the marginal ear vein under anesthesia. Hematological parameters were analyzed using an automated hematology analyzer to determine white blood cell (WBC) counts, red blood cell (RBC) counts and erythrocyte sedimentation rate (ESR). Serum C-reactive protein (CRP) levels were quantified using an enzyme-linked immunosorbent assay (ELISA). All measured parameters were compared with the established reference ranges for age-matched healthy rabbits.

After 12 weeks of implantation, the animals were euthanized, and the major organs, including the heart, liver, lungs, and kidneys, were harvested for histopathological evaluation. The tissues were fixed in 4% paraformaldehyde for 24 h, dehydrated through a graded ethanol series, embedded in paraffin, and sectioned into 4 μm-thick slices. Hematoxylin and eosin (H&E) staining was subsequently performed according to standard protocols. Histological examination was conducted under a light microscope to assess tissue architecture and identify potential pathological alterations, including inflammatory cell infiltration, tissue necrosis, fibrosis, and other abnormal

ACCEPTED PAPER

histological changes. All histopathological evaluations were independently performed by two experienced pathologists who were blinded to the experimental groups.

2.6. Statistical analysis

Animals were randomly assigned to experimental groups using a computer-generated randomization schedule. All imaging, histological, and quantitative analyses were performed by investigators blinded to group allocation. Data are presented as mean ± standard deviation (SD). Statistical analyses were performed using GraphPad Prism 10.0 (GraphPad Software, USA) and SPSS 26.0 (IBM Corp., USA). Differences among groups were analyzed using one-way ANOVA followed by Tukey's multiple-comparison test. Statistical differences are denoted as * ($p < 0.05$), ** ($p < 0.01$), and *** ($p < 0.001$).

3. Results

3.1. Characterizations of the cages

Two bioactive intervertebral cages, HA/Ti and Ta/PEEK, were successfully fabricated. Their macroscopic morphology are shown in **Figure.1**. All cages possessed identical dimensions (10 mm × 2 mm × 1.5 mm). Visual inspection revealed uniform coating coverage across the entire implant surface without visible cracking or delamination. The HA coating exhibited the characteristic dark-gray appearance of sintered calcium phosphate ceramics and completely covered the Ti substrate. In contrast, the Ta coating displayed a distinctive metallic luster with a dark metallic appearance. Both coatings markedly increased surface roughness relative to their uncoated counterparts.

SEM observations further revealed distinct microstructural characteristics of the two coatings (**Figure.1**). The HA coating consisted of densely stacked micron-scale lamellar crystals, generating a rough hierarchical surface favorable for protein adsorption and cellular anchorage. In contrast, the Ta-coated surface exhibited a more complex three-dimensional architecture characterized by irregular folds, protrusions, and nanoscale surface features. These topographical modifications substantially increased the effective surface area and generated favorable microenvironmental cues for subsequent cell attachment and tissue ingrowth.

ACCEPTED PAPER

The physicochemical properties of the cages were systematically characterized through compositional, wettability, mechanical, and structural analyses. EDS elemental mapping demonstrated homogeneous distributions of Ca, P, and O throughout the HA/Ti coating, whereas Ta was uniformly distributed across the Ta/PEEK surface (**Figures.2 and 3**), confirming excellent coating uniformity and compositional consistency. Contact-angle measurements revealed that the HA/Ti group exhibited the highest hydrophilicity among all groups, with a significantly reduced water contact angle (**Figure.4A, B**). Similarly, Ta deposition significantly decreased the contact angle of PEEK, indicating that both coating strategies effectively enhanced surface wettability. Mechanical testing demonstrated that neither coating process significantly altered the elastic modulus of the corresponding substrate material, indicating preservation of the intrinsic mechanical characteristics of the cages (**Figure.4C**). Porosity analysis further showed that both cage systems maintained highly interconnected porous architectures (**Figure.4D**). The Ti-based cages exhibited a porosity of approximately 55%, whereas the PEEK-based cages displayed a porosity of approximately 39%, with no significant alteration following surface modification.

Cross-sectional analyses demonstrated that both coatings possessed relatively uniform thickness distributions. The average thicknesses of the HA/Ti and Ta/PEEK coatings were approximately 570.6±14.9 nm and 650±34.8 nm, respectively (**Figure.5A, F**). Notably, the HA coating formed a distinct interface with the Ti substrate, with coating-associated elements primarily confined to the surface layer and limited elemental interdiffusion across the interface. In contrast, the Ta/PEEK system exhibited a gradual transition zone between the coating and substrate, accompanied by detectable elemental penetration into the underlying polymer matrix.

Scratch testing further highlighted the superior interfacial stability of the Ta coating (**Figure.5B, C, G, H**). The critical failure load and anti-delamination performance of the Ta/PEEK coating were substantially higher than those of the HA/Ti coating. The load–displacement curves of the HA/Ti samples exhibited pronounced fluctuations and abrupt force drops during scratching, indicating the occurrence of local microcracking and partial coating spallation under relatively low loads. In contrast, the Ta/PEEK coating displayed a smooth and continuous loading profile without sudden failure events. Furthermore, the HA/Ti coating reached its critical deformation threshold at an earlier stage, whereas the Ta/PEEK coating maintained structural integrity throughout a

ACCEPTED PAPER

larger loading range. These observations collectively indicate stronger interfacial bonding and enhanced mechanical robustness of the Ta coating.

Three-dimensional surface profilometry further revealed that the Ta/PEEK coating generated a well-organized hierarchical micro/nanostructure, whereas the HA/Ti surface displayed a comparatively irregular topography with randomly distributed depressions and protrusions (**Figure.5D, I**). Such ordered hierarchical features are generally considered advantageous for cellular attachment and spreading. XPS analysis further elucidated the surface chemical states of the coatings (**Figure.5E, J**). The HA/Ti coating exhibited characteristic signals corresponding to Ca^{2+} (Ca 2p, 347.3 eV) and PO_4^{3-} (P 2p, 133.3 eV), which are representative of hydroxyapatite. In contrast, the Ta/PEEK coating contained multiple tantalum oxidation states, including metallic Ta^0 (Ta 4f, 23.6 eV) and Ta^{5+} (Ta 4f,26.2 eV). The dominant Ta 4f signal corresponded to metal Ta, while partial surface oxidation indicated that tantalum oxide is formed in local areas.

3.2. Effects on cell viability, proliferation, and morphology

Biocompatibility is a prerequisite for the successful clinical application of implantable biomaterials[20]. Calcein-AM/propidium iodide (PI) live/dead staining (**Figure.6A**) revealed a homogeneous distribution of predominantly viable cells on all cage surfaces at both day 1 and day 3, with only sporadic dead cells observed. These findings indicate that none of the tested materials induced detectable cytotoxic effects. Moreover, the density of viable cells increased markedly from day 1 to day 3 in all groups, suggesting that the cages effectively supported early BMSCs survival and proliferation.

Cell viability was further quantified using a CCK-8 assay. As shown in **Figure.6D**, all groups exhibited a progressive increase in metabolic activity over time, with no significant differences among groups at the corresponding time points. These results further confirmed the excellent cytocompatibility of both coated and uncoated cages. Cell morphology and spreading behavior were subsequently evaluated by F-actin/DAPI staining. Representative fluorescence images (**Figure.6B, E**) demonstrated extensive cell spreading on all cage surfaces, accompanied by the formation of well-defined filopodia and lamellipodia. Such morphological features are characteristic of active cell–material interactions and indicate successful adhesion to the substrates. Quantitative analysis of F-actin extension revealed no statistically significant differences among

ACCEPTED PAPER

groups after 3 days of culture, suggesting that all materials provided a permissive microenvironment for initial cell attachment and cytoskeletal organization.

To further investigate the influence of surface modification on cell adhesion, the expression of adhesion-related molecules, including E-cadherin (CDH1) and integrin α2 (ITGα2), was analyzed by quantitative RT-PCR and immunofluorescence staining. As shown in **Figure.6C, F, G**, the Ta/PEEK group exhibited the highest mRNA expression levels of both CDH1 and ITGα2, followed by the HA/Ti group, whereas the Ti and PEEK groups showed progressively lower expression levels ($p < 0.05$). Consistent with the transcriptional results, immunofluorescence staining revealed markedly stronger CDH1 and ITGα2 signals in the Ta/PEEK group, moderate expression in the HA/Ti group, and relatively weak staining in the uncoated Ti and PEEK groups.

The enhanced expression of adhesion-associated molecules suggests that surface functionalization substantially improves cell–material interactions. Notably, the superior performance of the Ta/PEEK cage may be attributed to its hierarchical micro/nanostructured surface and favorable physicochemical properties, which collectively promote integrin-mediated cell anchorage and intercellular adhesion. These findings indicate that tantalum surface modification provides a more favorable adhesive microenvironment for BMSCs, thereby establishing a biological foundation for subsequent osteogenic differentiation and osseointegration.

3.3. Enhancing osteogenic ability

Evaluating the osteogenic activity induced by surface-engineered cages represents a central objective of this study[21]. Alkaline phosphatase (ALP), a hallmark enzyme associated with early osteogenic differentiation and extracellular matrix mineralization, was first assessed after 7 days of culture. As shown in **Figure.7A**, ALP staining revealed markedly enhanced osteogenic activity in the HA/Ti group compared with all other groups ($p < 0.05$). In contrast, no significant differences were observed among the Ti, PEEK, and Ta/PEEK groups. These findings were further corroborated by quantitative ALP activity measurements (**Figure 7D**), which demonstrated that the HA/Ti group exhibited significantly higher ALP activity than all other groups ($p < 0.05$), whereas the remaining groups displayed comparable levels.

To further investigate osteogenic commitment at the molecular level, the expression of osteogenesis-related genes was analyzed by RT-qPCR (**Figures.7F, G**). Consistent with the ALP

ACCEPTED PAPER

results, the HA/Ti group exhibited significantly elevated mRNA expression of Runx-2 and osteocalcin (OCN) relative to the other groups ($p < 0.05$). Immunofluorescence staining further confirmed these findings at the protein level. As shown in **Figures.7C, H and I**, the HA/Ti group displayed the strongest fluorescence intensity for both Runx-2 and OCN, whereas no marked differences were observed among the Ti, PEEK, and Ta/PEEK groups.

The ability of the cages to promote extracellular matrix mineralization was subsequently evaluated using Alizarin Red S (ARS) staining after 14 days of osteogenic induction (**Figure.7B, E**). Extensive calcium nodule formation was observed in the HA/Ti group, indicating enhanced mineral deposition. Quantitative analysis demonstrated that the absorbance value of the HA/Ti group was significantly higher than those of all other experimental groups ($p < 0.05$), while no significant differences were identified among the Ti, PEEK, and Ta/PEEK groups.

Collectively, these findings demonstrate that HA surface modification effectively enhances the osteogenic differentiation of BMSCs in vitro. The HA/Ti cages significantly increased ALP activity, upregulated the expression of key osteogenic markers, including Runx-2 and OCN, and promoted extracellular matrix mineralization. These results suggest that the HA coating provides potent osteoinductive and osteoconductive cues that facilitate early osteogenic commitment and matrix maturation.

3.4. Enhanced intervertebral fusion

To evaluate the osseointegration performance of the coated cages, vertebral specimens were harvested at 12 weeks postoperatively and subjected to micro-computed tomography (micro-CT) analysis. Three-dimensional reconstructions of the L4/L5 intervertebral space (**Figure.8A**) revealed pronounced bone formation in both the Ta/PEEK and HA/Ti groups, whereas bone ingrowth was relatively limited in the Ti and PEEK groups. Notably, discernible gaps between the cages and adjacent endplates were observed in the Ti and PEEK groups, indicating incomplete bone bridging at the bone–implant interface. Although the Ti group exhibited more evident subchondral bone formation at the inferior endplate compared with the PEEK group, both the HA/Ti and Ta/PEEK groups demonstrated direct and continuous osseointegration at the cage–endplate interface, suggesting substantially improved interfacial bone bonding relative to the uncoated controls.

ACCEPTED PAPER

Blinded radiographic fusion scoring further confirmed significant intergroup differences in fusion quality(**Figure.9C**). Overall, both the HA/Ti and Ta/PEEK groups exhibited the highest fusion scores, followed by the Ti group, while the PEEK group showed the poorest performance. The mean fusion scores of the HA/Ti and Ta/PEEK groups exceeded 2.0, indicating successful fusion according to the predefined scoring criteria. In contrast, only approximately half of the Ti group specimens achieved successful fusion criteria, reflecting moderate fusion efficiency, whereas the PEEK group exhibited consistently low scores, with minimal formation of intervertebral bone bridges. Quantitative micro-computed tomography (micro-CT) analysis further confirmed the osteogenic effects of the surface-engineered cages (**Figure.8B**). As shown by the reconstructed 3D images and quantitative parameters, both HA/Ti and Ta/PEEK groups exhibited significantly enhanced bone formation compared with the uncoated Ti and PEEK groups, as evidenced by increased trabecular number (Tb.N), bone volume fraction (BV/TV), and bone mineral density (BMD). Notably, the HA/Ti group showed better bone regenerative capacity than the Ta/PEEK group in BMD assessment. Although BV/TV and BMD differed significantly among groups, Tb.N showed no statistically significant intergroup difference. Collectively, these findings indicate that surface modification markedly enhances in vivo bone regeneration and confirms the critical role of interface engineering in promoting osseointegration.

Histological analysis using hematoxylin and eosin (H&E) staining revealed new bone and fibrocartilaginous tissue formation at the implant–bone interface and within the porous architecture of all experimental groups (**Figure.9A**). In terms of bone ingrowth, both HA/Ti and Ta/PEEK groups exhibited substantially greater newly formed bone area compared with the Ti and PEEK groups, accompanied by more continuous bone bridging across the implant interface. In contrast, the Ti and PEEK groups showed abundant fibrous tissue formation with limited new bone deposition, suggesting incomplete or unstable osseointegration. Notably, fibrous tissue encapsulation was frequently observed at the interface of Ti and PEEK cages, indicating poor osseointegration. Quantitative ImageJ analysis demonstrated bone ingrowth rates of 29.36 ± 1.82% (Ti), 42.31 ± 2.86% (HA/Ti), 25.16 ± 2.56% (PEEK), and 34.28 ± 1.62% (Ta/PEEK), respectively (**Figure.9B**). Statistical analysis confirmed that the HA/Ti group exhibited significantly higher bone ingrowth compared with the Ti and PEEK groups ($p < 0.001$) as well as the Ta/PEEK group ($p < 0.05$), while the PEEK group showed the lowest regenerative performance among all groups.

ACCEPTED PAPER

To further elucidate the biological mechanisms underlying in vivo bone regeneration and vascularization, immunohistochemical staining was performed at 12 weeks postoperatively to assess osteogenic and angiogenic marker expression (**Figure.9D, G, H**). The expression of osteogenesis-related proteins, including Runx-2 and OCN, showed marked intergroup differences. The HA/Ti group exhibited the strongest positive staining intensity and largest positive area, followed by the Ta/PEEK group, whereas the Ti and PEEK groups demonstrated progressively weaker expression, with the PEEK group showing the lowest levels ($p < 0.05$). These results indicate that HA/Ti modification provides the most potent osteoinductive microenvironment in vivo.

In contrast, angiogenesis-related markers revealed a different trend. CD31 and HIF-1α expression was significantly elevated in the Ta/PEEK group, which exhibited the highest microvessel density and the greatest number of HIF-1α-positive nuclei (**Figure.9D, E, F**). The HA/Ti group showed intermediate levels of angiogenic activity, whereas the Ti and PEEK groups demonstrated the lowest expression of both markers ($p < 0.05$). These findings suggest that Ta-based surface modification preferentially enhances neovascularization and may improve local oxygenation within the regenerative microenvironment.

Systemic biosafety was comprehensively evaluated through hematological analysis and histopathological examination of major organs, including the heart, liver, lungs, and kidneys (**Figure.10**). In all groups, white blood cell counts, red blood cell counts, CRP levels, and ESR values remained within physiological reference ranges, indicating the absence of detectable systemic inflammation or hematological abnormalities. Histological evaluation further demonstrated intact myocardial architecture, preserved hepatic lobular structure, normal alveolar morphology, and well-maintained renal glomerular and tubular structures in all animals. No evidence of inflammatory infiltration, tissue necrosis, fibrosis, or other pathological abnormalities was detected in any examined organ. These results collectively confirm that all implanted cages exhibit acceptable systemic biocompatibility without inducing detectable toxicity within the observation period.

4. Discussion

Previous studies have reported pseudarthrosis rates of approximately 5–35% after lumbar interbody fusion, depending on the number of fused segments, patient-related risk factors, and

ACCEPTED PAPER

implant design[22,23]. Such a high rate of nonunion is clinically relevant, as it is often associated with increased revision surgery rates and substantial healthcare burden[24]. Therefore, the development of bioactive intervertebral cages capable of reducing pseudarthrosis and promoting solid fusion remains of paramount importance. Among various strategies, surface coating engineering represents one of the most extensively investigated and clinically translatable approaches for orthopedic implants. In this study, hydroxyapatite (HA) and tantalum (Ta) were selected as coating materials due to their well-established biocompatibility and osteoconductive properties[25,26].

HA is widely recognized for its excellent bioactivity and structural similarity to native bone mineral, whereas tantalum has emerged as a promising candidate owing to its superior biocompatibility, corrosion resistance, and osseointegration potential. However, despite these advantages, clinical translation of Ta-coated PEEK cages has not yet been reported, largely due to the complexity and cost of coating fabrication, as well as unresolved technical challenges associated with coating adhesion on chemically inert PEEK substrates[27,28]. The inherently smooth and chemically stable surface of PEEK limits interfacial bonding with conventional coatings such as HA, thereby increasing the risk of delamination under frictional loading during implantation. In this context, Ta coating on PEEK offers a promising alternative strategy, which may preserve the favorable elastic modulus of PEEK while simultaneously imparting enhanced bioactivity and osteoconductivity derived from tantalum[29].

The elastic modulus of conventional solid titanium implants is significantly higher than that of both cortical and cancellous bone, which can lead to stress shielding effects[30]. Prolonged stress shielding may result in resorption and atrophy of subchondral trabecular bone, ultimately contributing to implant loosening, subsidence, and fusion failure[31]. In contrast, PEEK exhibits an elastic modulus closer to that of native bone, enabling more physiological load transfer and thereby reducing stress shielding–induced bone resorption and cystic changes. Accordingly, the primary rationale for introducing porosity into PEEK cages is not to further reduce its modulus, but rather to enhance biological performance and promote osseointegration. The porous architecture increases surface area, providing additional anchoring sites for cell adhesion, proliferation, and extracellular matrix deposition, while also facilitating nutrient transport and waste exchange[32-34]. However, excessive porosity inevitably compromises the mechanical

ACCEPTED PAPER

integrity of PEEK, whose tensile and flexural strengths are inferior to those of metallic materials. Therefore, an optimized, moderate porosity level is typically maintained to balance mechanical stability and biological functionality.

In this study, a previously established rabbit XLIF model was employed. A key advantage of this model is its ability to faithfully recapitulate the full clinical procedure of intervertebral disc removal, cage implantation, and internal fixation in a small-animal system. Specifically, the lateral approach allows the cage to be directly placed into the disc space, ensuring intimate contact between the cage surface and the adjacent vertebral endplates, thereby forming a physiologically relevant bone–implant interface. This configuration enables direct migration of cells from the vertebral endplate into the implant surface, closely mimicking the biological process of osseous ingrowth observed in clinical intervertebral fusion. In contrast, other small-animal models lacking a native endplate interface fail to reproduce this directional cellular migration, limiting their ability to evaluate true endplate–implant integration[35-37]. Compared with large-animal models, which are costly, time-consuming, and limited in sample size, this model significantly reduces experimental cost and accelerates research throughput[38]. It thus bridges the gap between in vitro studies and large-animal preclinical validation, providing an efficient platform for screening biomaterials and investigating osteogenic mechanisms[19].

Micro-CT and histological analyses demonstrated that, at early postoperative stages, both coating groups exhibited continuous and dense bone bridging at the bone–implant interface, with significantly greater new bone volume compared with the Ti group. These results highlight the osteoconductive function of the coatings. The chemical composition and crystalline structure of HA closely resemble native bone mineral, providing an ideal bioactive template for cell adhesion, proliferation, extracellular matrix deposition, and migration. In addition, HA surfaces facilitate protein adsorption and cell spreading, while also modulating the local microenvironment to upregulate osteogenic gene expression[39,40]. In contrast, Ta coating primarily promoted cell adhesion and early interfacial stabilization. Its unique surface characteristics facilitated rapid cell attachment and spreading, creating a favorable biological interface. Adsorbed extracellular matrix proteins on the Ta surface interact with integrin receptors on osteogenic cells, activating focal adhesion kinase (FAK) signaling and promoting cytoskeletal reorganization. These molecular events enhance initial adhesion strength and cell spreading capacity, thereby establishing a more

ACCEPTED PAPER

stable cell–material interface. Such reinforced adhesion is critical for the formation of durable bone–implant integration and subsequent osseointegration[41,42]. Although Ta/PEEK did not substantially promote osteogenic differentiation under simplified in vitro conditions, it enhanced fusion in vivo, likely through coordinated effects on early adhesion, angiogenesis, mechanical compatibility, and interfacial stability. The enhanced CD31 and HIF-1α expression suggests that Ta/PEEK may promote a pro-angiogenic microenvironment, indirectly supporting bone regeneration.

Overall, HA and Ta coatings represent two distinct yet complementary bioengineering strategies. The HA coating primarily functions through chemically and morphologically mediated bioactivity, with strong osteogenic and osteoconductive effects that upregulate osteogenic gene expression and accelerate early matrix mineralization[43,44]. Clinically, this translates into enhanced early fusion and faster bone bridging. In contrast, Ta/PEEK cages offer superior mechanical compatibility due to their elastic modulus being closer to cancellous bone, thereby mitigating stress shielding effects. Beyond mechanical advantages, Ta/PEEK also exhibited enhanced early vascularization, as evidenced by increased CD31 and HIF-1α expression, indicating improved neovascular ingrowth. Early vascularization provides essential oxygen, nutrients, and osteoprogenitor cell delivery, thereby accelerating the healing process at the bone–implant interface. Moreover, the microstructured Ta surface supports endothelial cell adhesion and spreading, which may further enhance VEGF secretion and establish a positive feedback loop that promotes angiogenesis. Although Ta surfaces may exhibit relatively lower intrinsic osteogenic activity in vitro compared with HA, their ability to regulate cellular adhesion and vascularization ultimately contributes to robust osseointegration in vivo[45,46].

Although autologous bone grafting remains the gold standard, its clinical application is limited by donor-site morbidity and insufficient availability. Alternative graft materials such as allografts and synthetic substitutes are associated with risks including immune rejection, disease transmission, and inconsistent osteogenic performance[47,48]. In contrast, the coating strategies developed in this study leverage intrinsic surface bioactivity to directly regulate and accelerate osseointegration, thereby reducing dependence on exogenous bone grafts. Furthermore, systemic biosafety is a critical prerequisite for clinical translation[49]. Our results demonstrated no significant histopathological abnormalities in major organs, nor any evidence of inflammatory

ACCEPTED PAPER

infiltration, tissue degeneration, or necrosis. Hematological parameters and inflammatory markers also remained within normal physiological ranges throughout the observation period. These findings collectively confirm the acceptable in vivo biocompatibility and systemic safety of both coating systems. Therefore, HA and Ta coating strategies provide a promising approach for achieving reliable intervertebral fusion without excessive reliance on bone graft materials, while maintaining sutiable biological safety.

Several limitations of this study should be acknowledged. First, although the rabbit XLIF model provides an efficient and clinically relevant platform for evaluating intervertebral fusion, it cannot fully replicate the biomechanical environment and healing characteristics of the human spine. Second, the observation period was limited to 12 weeks, and the long-term stability of the coating–implant interface as well as the durability of the fusion mass remain to be further investigated. Third, the molecular mechanisms underlying the enhanced angiogenic response observed in the Ta/PEEK group were not explored in depth. Future studies incorporating longer follow-up periods, large-animal models, and mechanistic analyses will be valuable for further validating the translational potential of these surface-engineered cages.

5. Conclusion

This study addresses the clinically relevant challenge of insufficient osseointegration associated with conventional intervertebral cages by developing and systematically evaluating surface coating strategies both in vitro and in vivo. The HA coating promotes osteogenesis through bioactive chemical cues, closely mimicking the composition of native bone mineral and thereby accelerating early-stage bone healing. In contrast, the Ta coating primarily provides an optimized interfacial architecture, combining a mechanically compatible elastic modulus with enhanced osteoconductive properties. This coating strategy demonstrated superior interfacial stability, increased surface roughness, and improved hydrophilicity, while preserving the structural integrity of the underlying substrate. Importantly, the Ta/PEEK cages facilitated enhanced cell adhesion and spreading, which was associated in vivo with enhanced angiogenic activity and improved intervertebral fusion. Collectively, this work presents translationally potent surface engineering strategies for developing next-generation bioactive intervertebral fusion devices that overcome the intrinsic biological inertness of conventional implant materials.

ACCEPTED PAPER

Acknowledgments

We thank all of the participants for their help and support.

Funding

This work was supported by 2024 Hebei Provincial Traditional Chinese Medicine Scientific Research Project Plan [grant number 2024045]; 2025 Hebei Provincial Medical Applicable Technology Tracking Project [grant number GZ20250025]; 2026 Hebei Provincial Higher Education Scientific Research Project [grant number CXZX2026045].

Conflict of interest

The authors declare that they have no known competing financial interests or personal relationships that could have appeared to influence the work reported in this paper.

Author contributions

Conceptualization: Shaorong Li, Lei Ma, Wei Zhang

Formal analysis: Hongwei Gao, Xiuqi, Shan

Investigation: Han Wu, Jianshi Song

Methodology: Shaorong Li

Writing–original draft: Shaorong Li

Writing–review & editing: Jiaqi Li, Lei Ma, Wei Zhang

Ethics approval and consent to participate

All animal experiments were approved by the Animal Protection and Experiment Committee of Hebei Medical University and conducted in accordance with international animal welfare guidelines (Ethical number: Z2025-046-1).

Consent for publication

Not applicable.

ACCEPTED PAPER

Availability of data

Data are available from the corresponding author upon reasonable request.

References

[1] Kotheeranurak V, Jitpakdee K, Lin GX, et al. Subsidence of Interbody Cage Following Oblique Lateral Interbody Fusion: An Analysis and Potential Risk Factors. Global Spine J. Sep 2023;13(7):1981-1991. doi:10.1177/21925682211067210

[2] Xuan W, Cheng Q, Gao Y, Song Z, Gao Z. Early-stage lumbar paraspinal muscle injury: endoscopic versus transforaminal lumbar interbody fusion: a retrospective comparative analysis. J Orthop Surg Res. Sep 26 2025;20(1):841. doi:10.1186/s13018-025-06235-8

[3] Zhou H, Bian H, Zhang Y, et al. Evaluation of Indirect Decompression Effect After Extreme Lateral Lumbar Interbody Fusion Using Three-Dimensional Volumetric Measurements-A Retrospective Study. Orthop Surg. Sep 2025;17(9):2558-2569. doi:10.1111/os.70108

[4] Wu H, Shan Z, Zhao F, Cheung JPY. Poor Bone Quality, Multilevel Surgery, and Narrow and Tall Cages Are Associated with Intraoperative Endplate Injuries and Late-onset Cage Subsidence in Lateral Lumbar Interbody Fusion: A Systematic Review. Clin Orthop Relat Res. Jan 1 2022;480(1):163-188. doi:10.1097/corr.0000000000001915

[5] Burkhard MD, Guven AE, Demopoulos B, et al. 3D-Printed Titanium: Game-Changer for Standalone Lateral Lumbar Interbody Fusion? An Analysis of Risk Factors for Revision Surgery. Global Spine J. Sep 29 2025:21925682251383879. doi:10.1177/21925682251383879

[6] Schnake KJ, Fleiter N, Hoffmann C, et al. PLIF with titanium-coated versus uncoated PEEK cages: a prospective randomized clinical trial. Eur Spine J, 2021,30(1):114-121. doi.org/10.1007/s00586-020-06642-x

[7] Jain S, Eltorai AE, Ruttiman R, Daniels AH. Advances in Spinal Interbody Cages. Orthop Surg. 2016;8(3):278-284. doi:10.1111/os.12264

ACCEPTED PAPER

[8] Zhang Y, Yang J, Wan W, et al. Evaluation of biological performance of 3D printed trabecular porous tantalum spine fusion cage in large animal models. J Orthop Translat. Jan 2025;50:185-195. doi:10.1016/j.jot.2024.10.010

[9] He X, Li Y, Zou D, Zu H, Li W, Zheng Y. An overview of magnesium-based implants in orthopaedics and a prospect of its application in spine fusion. Bioact Mater. Sep 2024;39:456-478. doi:10.1016/j.bioactmat.2024.04.026

[10] Zhang H, Gao G, Wang L, et al. Innovative 3D-printed porous piezoelectric poly(vinylidene fluoride) cages with accelerated spinal fusion. Mater Today Bio. Dec 2025;35:102333. doi:10.1016/j.mtbio.2025.102333

[11] Wu H, Dong H, Tang Z, et al. Electrical stimulation of piezoelectric BaTiO3 coated Ti6Al4V scaffolds promotes anti-inflammatory polarization of macrophages and bone repair via MAPK/JNK inhibition and OXPHOS activation. Biomaterials. Feb 2023;293:121990. doi:10.1016/j.biomaterials.2022.121990

[12] Zheng H, Cheng F, Guo D, He X, Zhou L, Zhang Q. Nanoenzyme-Reinforced Multifunctional Scaffold Based on Ti(3)C(2)Tx MXene Nanosheets for Promoting Structure-Functional Skeletal Muscle Regeneration via Electroactivity and Microenvironment Management. Nano Lett. Aug 23 2023;23(16):7379-7388. doi:10.1021/acs.nanolett.3c01784

[13] Luo L, Zheng W, Li J, et al. 3D-Printed Titanium Trabecular Scaffolds with Sustained Release of Hypoxia-Induced Exosomes for Dual-Mimetic Bone Regeneration. Adv Sci (Weinh). Jun 2025;12(23):e2500599. doi:10.1002/advs.202500599

[14] Lin R, Wang Z, Li Z, Gu L. A two-phase and long-lasting multi-antibacterial coating enables titanium biomaterials to prevent implants-related infections. Mater Today Bio. Jun 2022;15:100330. doi:10.1016/j.mtbio.2022.100330

[15] Coppola B, Montanaro L, Palmero P. DLP Fabrication of Zirconia Scaffolds Coated with HA/β-TCP Layer: Role of Scaffold Architecture on Mechanical and Biological Properties. Journal of Functional Biomaterials. Sep 2022;13(3)148. doi:10.3390/jfb13030148

[16] Sun T, Huang H, Zhao Y, Li Z, Wang H, Zhou G. Low-Temperature Deposited Amorphous Poly(aryl ether ketone) Hierarchically Porous Scaffolds with Strontium-Doped Mineralized

ACCEPTED PAPER

Coating for Bone Defect Repair. Adv Healthc Mater. Sep 2024;13(23):e2400927. doi:10.1002/adhm.202400927

[17] Durham JW, 3rd, Rabiei A. Deposition, Heat Treatment And Characterization of Two Layer Bioactive Coatings on Cylindrical PEEK. Surf Coat Technol. Sep 15 2016;301:106-113. doi:10.1016/j.surfcoat.2015.12.045

[18] Torstrick FB, Lin ASP, Potter D, et al. Porous PEEK improves the bone-implant interface compared to plasma-sprayed titanium coating on PEEK. Biomaterials. Dec 2018;185:106-116. doi:10.1016/j.biomaterials.2018.09.009

[19] Li J, Zhao B, Wang W, Xu Y, Wu H, Zhang W. Improved intervertebral fusion in LLIF rabbit model with a novel titanium cage. Spine J. Jun 2024;24(6):1109-1120. doi:10.1016/j.spinee.2023.12.011

[20] Guillot R, Pignot-Paintrand I, Lavaud J, et al. Assessment of a polyelectrolyte multilayer film coating loaded with BMP-2 on titanium and PEEK implants in the rabbit femoral condyle. Acta Biomater. May 2016;36:310-22. doi:10.1016/j.actbio.2016.03.010

[21] Zhang J, Ma T, Liu X, Zhang X, Meng W, Wu J. Multifunctional surface of the nano-morphic PEEK implant with enhanced angiogenic, osteogenic and antibacterial properties. Regen Biomater. 2024;11:rbae067. doi:10.1093/rb/rbae067

[22] An J, Shi X, Zhang J, et al. Dual aldehyde cross-linked hyaluronic acid hydrogels loaded with PRP and NGF biofunctionalized PEEK interfaces to enhance osteogenesis and vascularization. Mater Today Bio. Feb 2024;24:100928. doi:10.1016/j.mtbio.2023.100928

[23] Adl Amini D, Okano I, Oezel L, et al. Evaluation of cage subsidence in standalone lateral lumbar interbody fusion: novel 3D-printed titanium versus polyetheretherketone (PEEK) cage. Eur Spine J. 2021;30(8):2377-2384. doi:10.1007/s00586-021-06912-2

[24] Mahjoubi H, Buck E, Manimunda P, et al. Surface phosphonation enhances hydroxyapatite coating adhesion on polyetheretherketone and its osseointegration potential. Acta Biomater. Jan 1 2017;47:149-158. doi:10.1016/j.actbio.2016.10.004

ACCEPTED PAPER

[25] Zhang W, Shi D, Huang S, Li S, Zeng M, Wei Y. Personalised 3D-printed bioactive peek bone plate scaffold for treating femoral defects. RSC Adv. Feb 13 2025;15(7):5060-5072. doi:10.1039/d4ra07573k

[26] Xu J, Wu D, Ge B, et al. Selective Laser Melting of the Porous Ta Scaffold with Mg-Doped Calcium Phosphate Coating for Orthopedic Applications. ACS Biomater Sci Eng. Mar 11 2024;10(3):1435-1447. doi:10.1021/acsbiomaterials.3c01503

[27] Zhu C, He M, Mao L, et al. Titanium interlayer-mediated hydroxyapatite-coated polyetheretherketone cage in transforaminal lumbar interbody fusion surgery. BMC Musculoskelet Disord. 2021;22(1):918. doi:10.1186/s12891-021-04803-7

[28] Jia CQ, Zhang Z, Cao SQ, et al. A biomimetic gradient porous cage with a micro-structure for enhancing mechanical properties and accelerating osseointegration in spinal fusion. Bioact Mater. 2022;23:234-246. doi:10.1016/j.bioactmat.2022.11.003

[29] Ragni E, Perucca Orfei C, Bidossi A, et al. Superior Osteo-Inductive and Osteo-Conductive Properties of Trabecular Titanium vs. PEEK Scaffolds on Human Mesenchymal Stem Cells: A Proof of Concept for the Use of Fusion Cages. Int J Mol Sci. 2021;22(5):2379. doi:10.3390/ijms22052379

[30] Laubach M, Kobbe P, Hutmacher DW. Biodegradable interbody cages for lumbar spine fusion: Current concepts and future directions. Biomaterials. Sep 2022;288:121699. doi:10.1016/j.biomaterials.2022.121699

[31] Mobbs RJ, Phan K, Assem Y, Pelletier M, Walsh WR. Combination Ti/PEEK ALIF cage for anterior lumbar interbody fusion: Early clinical and radiological results. J Clin Neurosci. 2016;34:94-99. doi:10.1016/j.jocn.2016.05.028

[32] Park PJ, Lehman RA. Optimizing the Spinal Interbody Implant: Current Advances in Material Modification and Surface Treatment Technologies. Curr Rev Musculoskelet Med. 2020;13(6):688-695. doi:10.1007/s12178-020-09673-5

[33] Lu T, Wen J, Qian S, et al. Enhanced osteointegration on tantalum-implanted polyetheretherketone surface with bone-like elastic modulus. Biomaterials. 2015;51:173-183. doi:10.1016/j.biomaterials.2015.02.018

ACCEPTED PAPER

[34] Hwangbo H, Lee J, Kim G. Mechanically and biologically enhanced 3D-printed HA/PLLA/dECM biocomposites for bone tissue engineering. Int J Biol Macromol. Oct 1 2022;218:9-21. doi:10.1016/j.ijbiomac.2022.07.040

[35] Blom AM, Petersen EB, A Grieser-Yoder R, R Olinger C, Fredericks DC. A Novel Nano-Synthetic Hydrophilic Bone Graft (OsteoFlo HydroFiber) Is a Non-inferior Alternative to Iliac Crest Autograft in a Rabbit Posterolateral Fusion Model. Global Spine J. April 20, 2026. doi:10.1177/21925682261442308

[36] Jin YZ, Zheng GB, Cho M, Lee JH. Effect of Whitlockite as a new bone substitute for bone formation in spinal fusion and ectopic ossification animal model. Biomater Res. 2021;25(1):34. doi:10.1186/s40824-021-00237-3

[37] Ryan DA, Cheng J, Masuda K, Cashman JR. Role of Curcuminoids and Tricalcium Phosphate Ceramic in Rat Spinal Fusion. Tissue Eng Part C Methods. 2020;26(11):577-589. doi:10.1089/ten.TEC.2020.0217

[38] Sun J, Liu SS, Zou D, et al. A novel porous interbody fusion cage modified by microarc oxidation and hydrothermal treatment technology accelerate osseointegration and spinal fusion in sheep. RSC Adv. 2024;14(44):31966-31978. doi:10.1039/d3ra08185k

[39] Tian L, Zhang Z, Tian B, Zhang X, Wang N. Study on antibacterial properties and cytocompatibility of EPL coated 3D printed PCL/HA composite scaffolds. RSC Adv. Jan 24 2020;10(8):4805-4816. doi:10.1039/c9ra10275b

[40] Liu B, Ma Z, Li J, et al. Experimental study of a 3D printed permanent implantable porous Ta-coated bone plate for fracture fixation. Bioact Mater. Apr 2022;10:269-280. doi:10.1016/j.bioactmat.2021.09.009

[41] Liu T, Li B, Chen G, Ye X, Zhang Y. Nano tantalum-coated 3D printed porous polylactic acid/beta-tricalcium phosphate scaffolds with enhanced biological properties for guided bone regeneration. Int J Biol Macromol. Nov 30 2022;221:371-380. doi:10.1016/j.ijbiomac.2022.09.003

[42] Tao Y, Jia M, Shao-Qiang Y, et al. A novel fluffy PLGA/HA composite scaffold for bone defect repair. J Mater Sci Mater Med. Mar 15 2024;35(1):16. doi:10.1007/s10856-024-06782-2

ACCEPTED PAPER

[43] Duan W, Chen C, Haque M, Hayes D, Lopez MJ. Polymer-mineral scaffold augments in vivo equine multipotent stromal cell osteogenesis. Stem Cell Res Ther. Mar 9 2018;9(1):60. doi:10.1186/s13287-018-0790-8

[44] Chi H, Chen G, He Y, et al. 3D-HA Scaffold Functionalized by Extracellular Matrix of Stem Cells Promotes Bone Repair. Int J Nanomedicine. 2020;15:5825-5838. doi:10.2147/ijn.S259678

[45] Zhang K, Hu H, Sun Y, et al. The bio-functionalized membrane loaded with Ta/WH nanoparticles promote bone regeneration through neurovascular coupling. Colloids Surf B Biointerfaces. Oct 2023;230:113506. doi:10.1016/j.colsurfb.2023.113506

[46] Baldwin P, Li DJ, Auston DA, Mir HS, Yoon RS, Koval KJ. Autograft, Allograft, and Bone Graft Substitutes: Clinical Evidence and Indications for Use in the Setting of Orthopaedic Trauma Surgery. J Orthop Trauma. Apr 2019;33(4):203-213. doi:10.1097/bot.0000000000001420

[47] Gupta A, Kukkar N, Sharif K, Main BJ, Albers CE, El-Amin Iii SF. Bone graft substitutes for spine fusion: A brief review. World J Orthop. 2015;6(6):449-456. doi:10.5312/wjo.v6.i6.449

[48] Zhang J, Tong D, Song H, et al. Osteoimmunity-Regulating Biomimetically Hierarchical Scaffold for Augmented Bone Regeneration. Adv Mater. Sep 2022;34(36):e2202044. doi:10.1002/adma.202202044

[49] Deshpande R, Shukla S, Kale A, Deshmukh N, Nisal A, Venugopalan P. Silk Fibroin Microparticle Scaffold for Use in Bone Void Filling: Safety and Efficacy Studies. ACS Biomater Sci Eng. Mar 14 2022;8(3):1226-1238. doi:10.1021/acsbiomaterials.1c01103

ACCEPTED PAPER

Figures and Tables

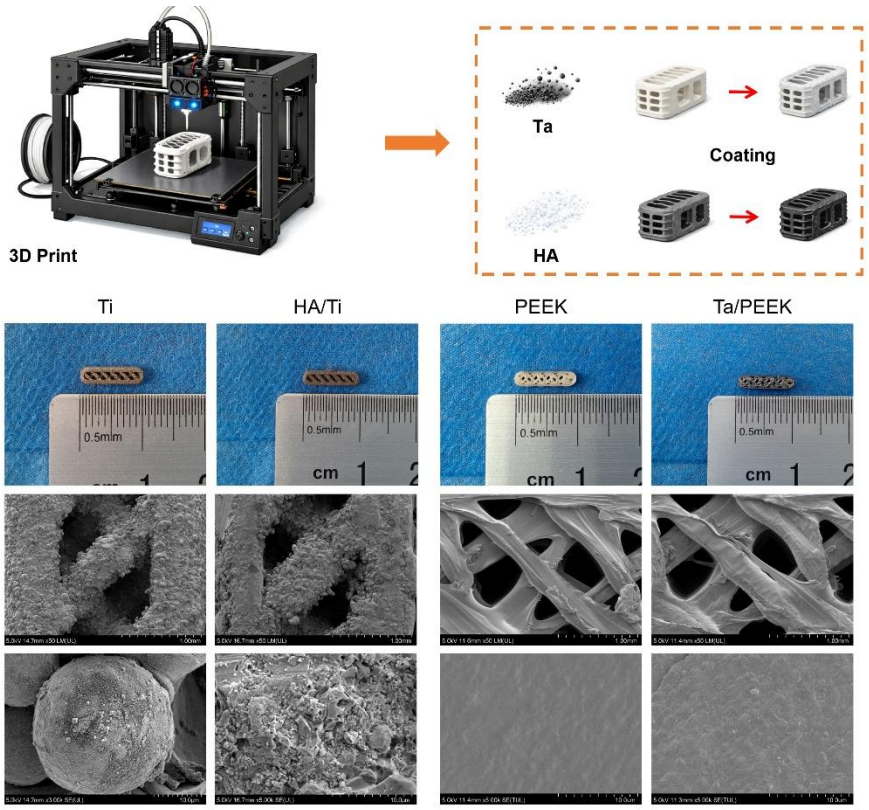


Figure.1 Fabrication and microstructure observation of each cage.(The scales in the image correspond to 1 mm and 10 microns respectively).

ACCEPTED

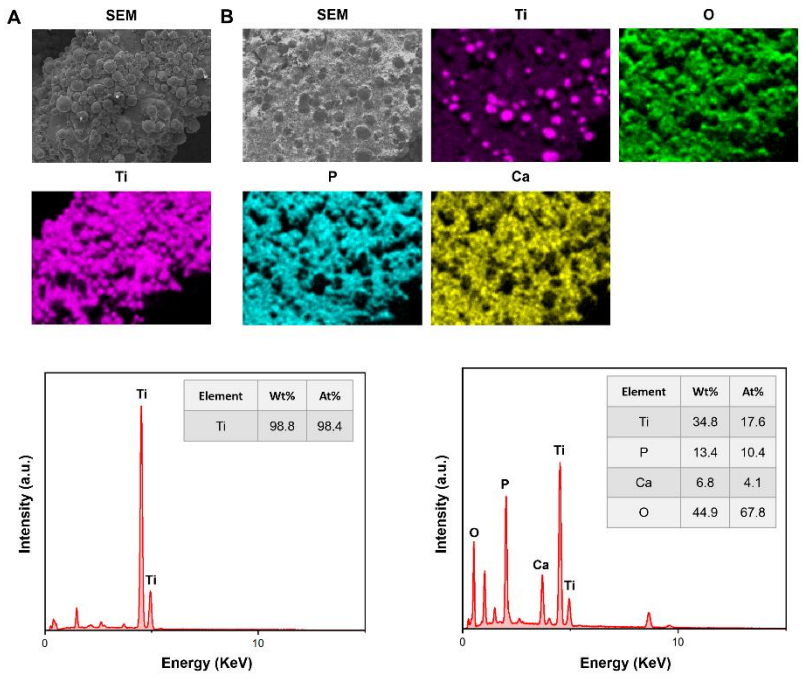


Figure.2 Elemental scanning and quantitative analysis of Ti(A) and HA/Ti cage(B) surfaces.

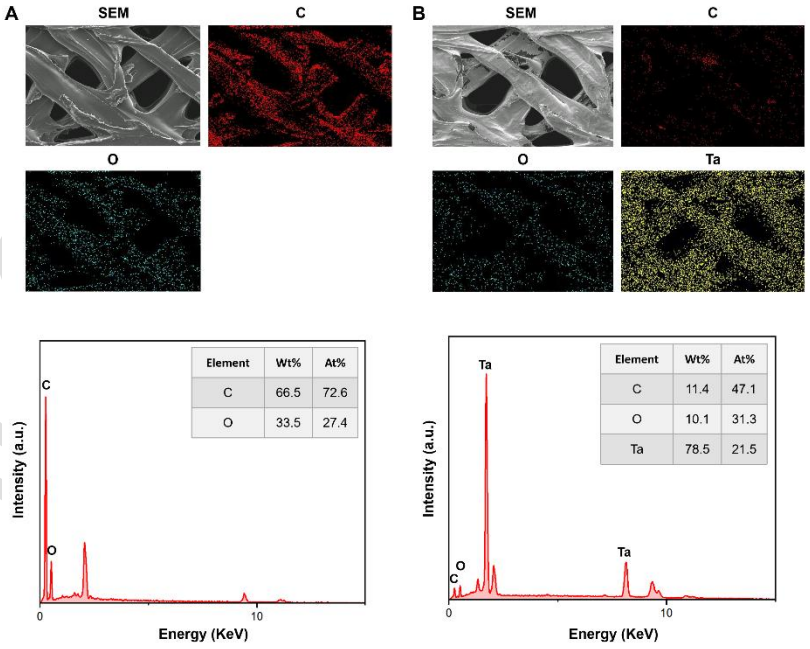


Figure.3 Elemental scanning and quantitative analysis of PEEK (A) and Ta/PEEK cage (B) surfaces.

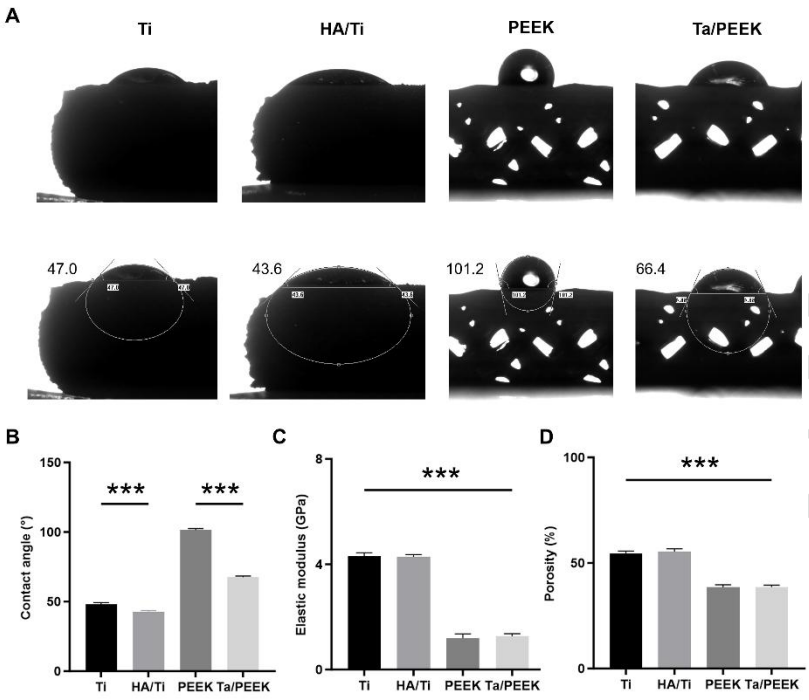


Figure.4 Analysis of contact angle (A, B), elastic modulus (C) and porosity (D) of each cage. (n = 3, * indicates significant difference between groups, * $p < 0.05$, ** $p < 0.01$, *** $p < 0.001$)

ACCEPTED MANUSCRIPT

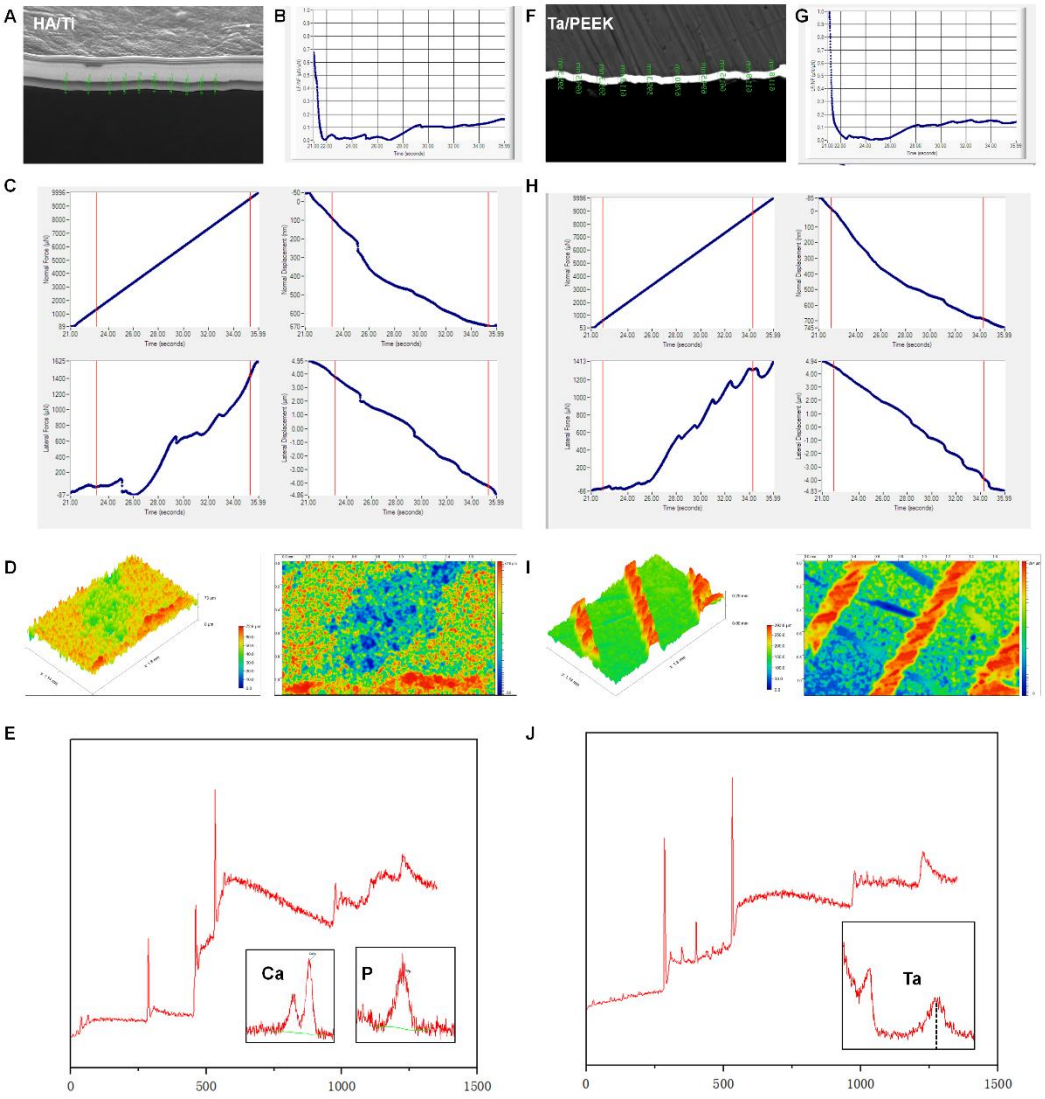


Figure.5. Characterization of coating properties for the two coating cages. (A) Coating thickness of the HA/Ti cage. (B, C) Interfacial bonding strength of the HA/Ti cage. (D) Three-dimensional surface profilometry of the HA/Ti cage. (E) XPS characterization of the HA/Ti cage. (F) Coating thickness of the Ta/PEEK cage. (G, H) Interfacial bonding strength of the Ta/PEEK cage. (I) Three-dimensional surface profilometry of the Ta/PEEK cage. (J) XPS characterization of the Ta/PEEK cage.

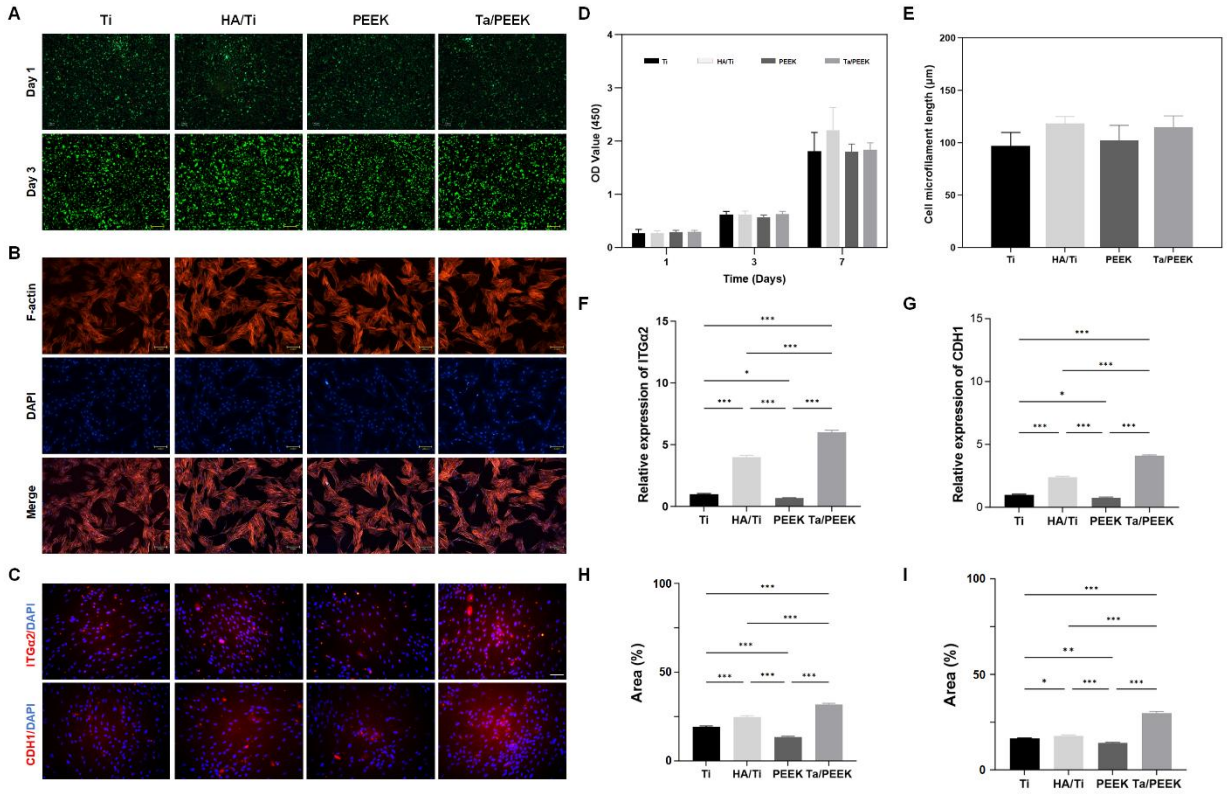


Figure.6 In vitro biocompatibility and cell adhesion of the cages. (A) Representative live/dead staining images of BMSCs cultured on the different cages at days 1 and 3. Scale bar: 500 μm. (B) Representative F-actin/DAPI staining images of BMSCs cultured on the different cages at day 3. Scale bar: 100 μm. (C) Representative immunofluorescence staining images of the adhesion-related proteins ITGα2 and CDH1 in BMSCs cultured on the different cages. Scale bar: 100 μm. (D) Quantitative assessment of BMSC proliferation on the different cages at days 1, 3, and 7. (E) Quantification of F-actin length in BMSCs cultured on the different cages. (F, G) Relative mRNA expression levels of ITGα2 (F) and CDH1 (G) in BMSCs cultured on the different cages. (H, I) Semi-quantitative analysis of ITGα2 (H) and CDH1 (I) immunofluorescence intensity. (n = 3, * indicates significant difference between groups, * $p < 0.05$, ** $p < 0.01$, *** $p < 0.001$)

ACCEPTED

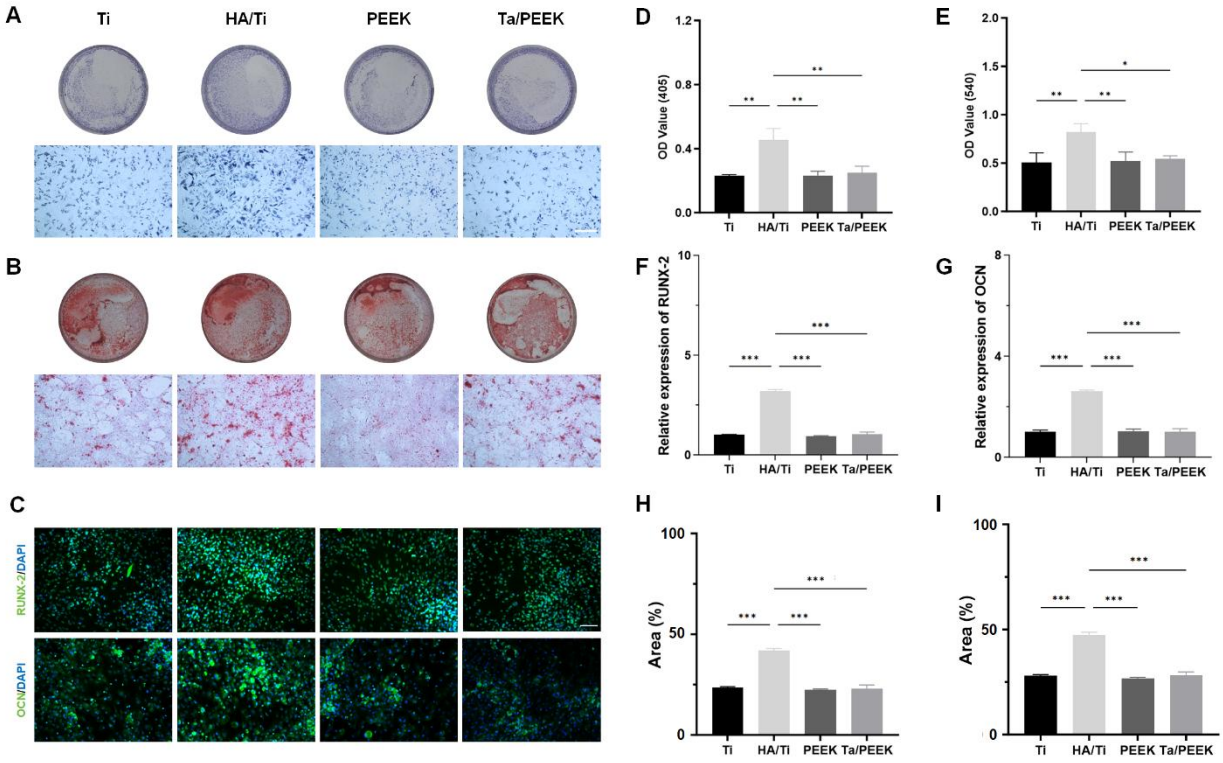


Figure.7 Evaluation of the osteogenic differentiation of BMSCs induced by the different cages. (A, B) Representative ALP staining (A) images at day 7 and ARS staining (B)images at day 14. Scale bars: 500 μm. (C) Representative immunofluorescence staining images of the osteogenic proteins Runx-2 and OCN in BMSCs cultured on the different cages. Scale bar: 100 μm. (D) Quantification of ALP activity at day 7. (E) Semi-quantitative analysis of mineralized matrix formation based on ARS staining at day 14. (F, G) Relative mRNA expression levels of the osteogenic genes Runx-2 (F) and OCN (G). (H, I) Semi-quantitative analysis of Runx-2 (H) and OCN (I) immunofluorescence intensity. (n = 3, * indicates significant difference between groups, * $p < 0.05$, **$p < 0.01$, ***$p < 0.001$)

ACCEPTED

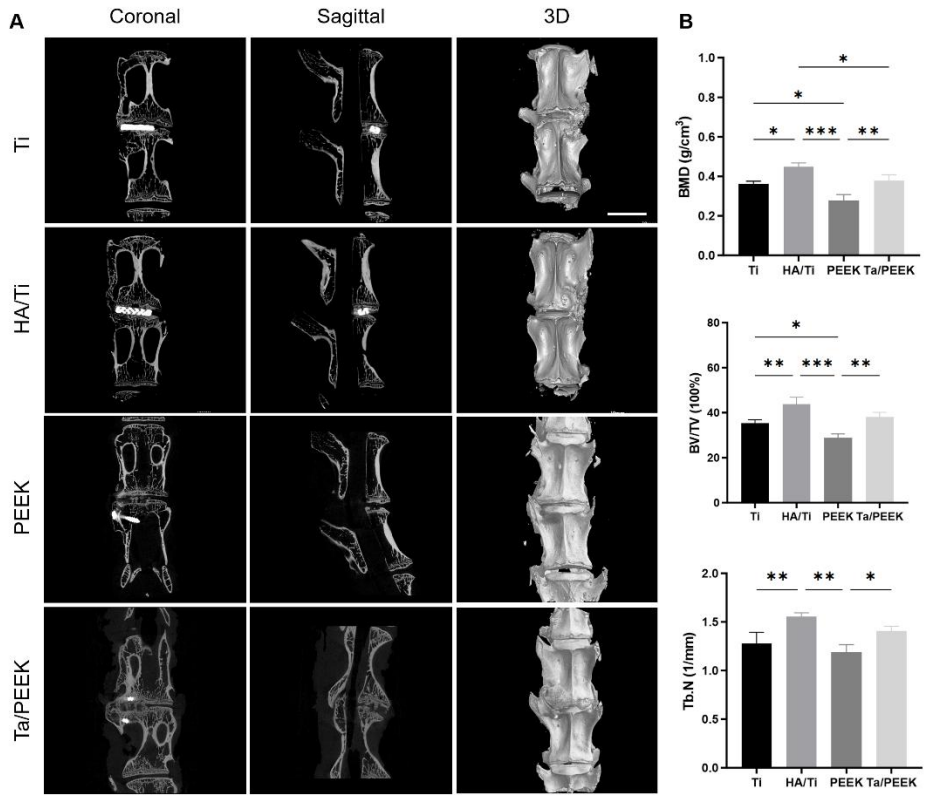


Figure.8 Micro-CT evaluation of intervertebral fusion at 12 weeks post-surgery. (A) Representative micro-CT images of the L4–L5 intervertebral region in each group. Scale bar = 10 mm. (B) Semi-quantitative analysis of intervertebral fusion among the different groups. (n = 6, * indicates significant difference between groups, * $p < 0.05$, **$p < 0.01$, ***$p < 0.001$)

ACCEPTED

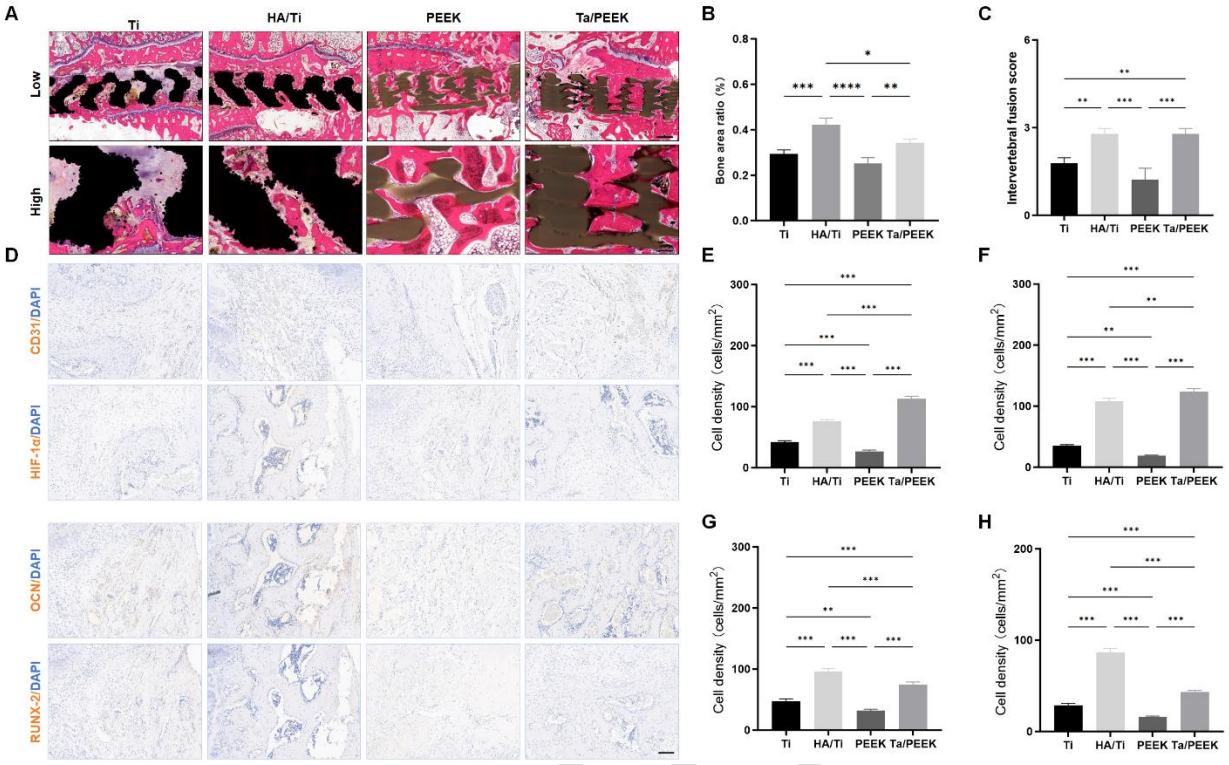


Figure.9 Histological assessment of intervertebral fusion and new bone formation at 12 weeks post-surgery. (A) Representative H&E staining images of the L4–L5 fusion segment. Scale bars: 1000 μm and 250 μm, respectively. (B) Semi-quantitative histological evaluation of the fusion tissues. (C) Fusion scores of the different groups at 12 weeks post-surgery. (D) Representative immunohistochemical staining images of CD31 and HIF-1α, Runx-2 and OCN in newly formed bone within the fusion region. Scale bar: 100 μm. (E, F) Semi-quantitative analysis of CD31 (E) and HIF-1α (F) expression. (G, H) Semi-quantitative analysis of OCN (G) and Runx-2 (H) expression. (n = 6, * indicates significant difference between groups, * $p < 0.05$, **$p < 0.01$, ***$p < 0.001$)

ACCEPTED

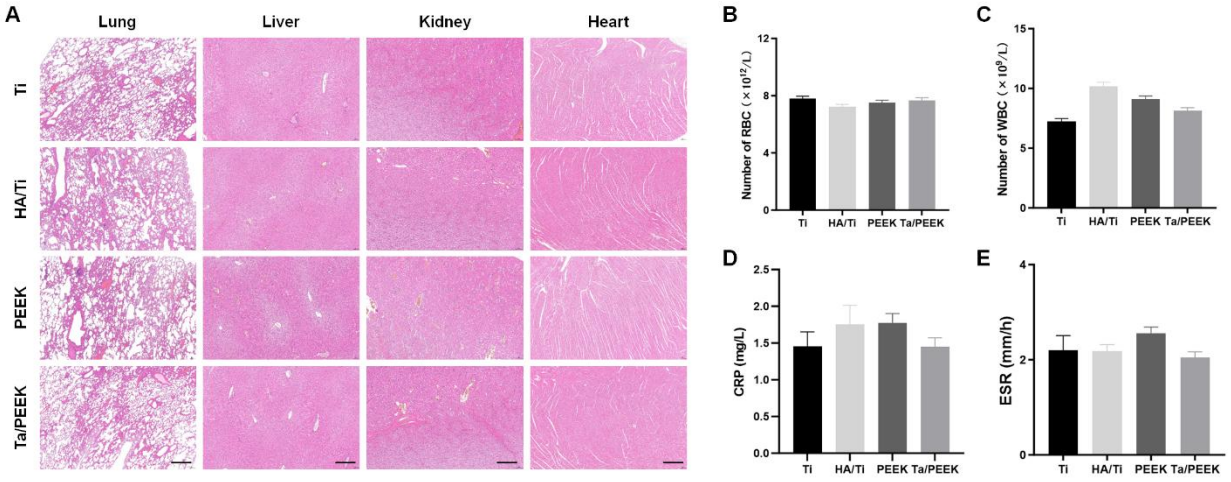


Figure.10 In vivo biosafety assessment of the cages. (A) Representative H&E staining images of major organs, including the heart, liver, lung, and kidney, harvested at 12 weeks post-surgery. Scale bars: 50 μm (heart, lung, and kidney) and 25 μm (liver). (B, C) Quantitative analysis of peripheral blood red blood cell (RBC) and white blood cell (WBC) counts in rabbits at 4 weeks post-surgery. (D, E) Quantification of inflammatory indicators, including C-reactive protein (CRP) and erythrocyte sedimentation rate (ESR), in peripheral blood at 4 weeks post-surgery. (n = 6, Because hematological and inflammatory parameters vary among individual animals, statistical comparisons were not emphasized. Values outside the physiological reference ranges were considered abnormal; no abnormal values were detected in any group.)

ACCEPTED PAPER

Table. 1 The primer sequences used for RT-qPCR.

Gene subtype	Oligonucleotide Primers (5'-3')
CDH1	F: CAGTGTTTGCTCGGCGTTT
	R: CGCCCTTTTGATTTTCCGGG
ITGα2	F:ACCCTTTGGATCTGCGAGTG
	R:AGAAAACTCAGCCAGGACGG
OCN	F: CCTAGCAGACACCATGAGGAC
	R: GCTTGGACATGAAGGCTTTGTC
Runx-2	F: AGAGTCAGATTACAGATCCCAGG
	R: TGGCTCTTCTTACTGAGAGAGG
GAPDH	F: CACCATCTTCCAGGAGCGAG
	R: GGCGGAGATGATGACCCTTT